Characterisation of steel corrosion and matrix damage in reinforced mortar combining analytical, electrical and image-based techniques

Cement and Concrete Research 190 (2025) 107792

Contents lists available at ScienceDirect

Cement and Concrete Research

journal homepage: www.elsevier.com/locate/cemconres

Characterisation of steel corrosion and matrix damage in reinforced mortar combining analytical, electrical and image-based techniques

Andreas Alhede [a,*], Jelke Dijkstra [a], Alessandro Tengattini [b,c,d], Karin Lundgren [a]

[a] Chalmers University of Technology, Gothenburg, Sweden
[b] Institut Laue-Langevin, Grenoble, France
[c] Univ. Grenoble Alpes, Grenoble INP, CNRS, 3SR, 1270 Rue de la Piscine, Grenoble, 38400, France
[d] Institut universitaire de France (IUF), France

ARTICLE INFO

Dataset link: https://dx.doi.org/10.5291/ILL-DATA.1-07-1

Keywords:
Steel corrosion
Steel-concrete interface
Macroscopic interfacial voids
X-ray computed tomography
Neutron computed tomography

ABSTRACT

Characterising steel corrosion at the steel-concrete interface and linking it to concrete damage is challenging due to limitations of current non-destructive techniques. This study combines electrical resistance measurements, full-field image-based analyses and analytical techniques to comprehensively characterise steel corrosion and damage in small-scale specimens.

X-ray and Neutron Computed Tomography of two reinforced mortar samples, before and after accelerated corrosion, were used to examine corrosion morphology, interfacial voids, and estimate volumetric strain in the corrosion layer. Inductively Coupled Plasma Mass Spectrometry was employed to measure iron isotope concentrations in water surrounding the specimens.

The results revealed delayed transport of corrosion products relative to mortar cracking. The volumetric expansion coefficients of corrosion products (3.84 and 3.90) align with previous research, and the risk of pitting corrosion correlated with the void size. Overall, the measurements obtained through the various techniques closely aligned with visual observations, providing a robust dataset for calibrating corrosion models.

1. Introduction

Assessment of steel corrosion in Reinforced Concrete (RC) structures poses a significant challenge in the field of civil engineering. In the case of chloride-induced corrosion, which is typical for structures located in a marine environment or subjected to de-icing salts, chloride ions diffuse into the concrete cover and disrupt the passive film that initially protects the reinforcement against oxidation [1]. Once depassivated, steel corrosion becomes active in the presence of oxygen and water [2].

The oxidation process leads to reduced cross-sectional area of the steel, potentially impacting its load-bearing capacity, tensile ductility [3] and fatigue performance [4]. Additionally, the formation of corrosion products at the Steel-Concrete Interface (SCI) results in a volume increase, which may lead to cracking of the concrete cover due to the significant pressure exerted.

These cracks potentially accelerate further deterioration of the SCI, by providing pathways for ingress of aggressive agents, such as chlorides. When cracking occurs in anchorage regions, the bond strength is reduced, subsequently affecting the anchorage capacity of the structure. Therefore, understanding of the mechanisms and physical processes of steel corrosion in RC structures is crucial for effectively predicting their durability and long-term performance.

Extensive research efforts have been invested in developing models to predict the corrosion and cracking process, at various level of detail (see for example [5–8]). However, these models often are phenomenological relying on non-physical model parameters that significantly affect their outputs. While these models are calibrated to specific experimental conditions and provide reasonable outputs for those conditions, their performance generally declines when applied to different experiments [9]. This is due to the calibration being tailored to the original conditions, which limits the broader applicability of the models.

Experimental data is required to better understand the processes adjacent to SCI, so as to overcome the aforementioned modelling limitations, and develop physics-based models for steel corrosion in RC. A significant challenge, however, lies in the destructive nature of most experimental techniques, complicating the *evolution* of corrosion characteristics and the influence of the multiple driving factors at the SCI.

Previous studies on the composition of corrosion products in RC have identified oxides such as goethite, lepidocrosite, magnetite and maghemite [10,11]. These corrosion products exhibit varying free volumetric expansions, ranging from 2 to 6 times the volume of the

* Corresponding author.
E-mail address: andreas.alhede@chalmers.se (A. Alhede).

https://doi.org/10.1016/j.cemconres.2025.107792
Received 2 October 2024; Received in revised form 11 January 2025; Accepted 16 January 2025
Available online 30 January 2025

consumed steel [2]. Thus, the types of oxides formed significantly affects the pressure exerted on the concrete cover and is consequently an essential factor to understand for accurate modelling of the corrosion and cracking process.

Beside understanding how different corrosion products influence pressure build-up at the SCI, it is also crucial to investigate their morphology. Previous destructive research suggests that macroscopic interfacial voids may increase the risk of pitting corrosion. In particular, the size of these voids appears to correlate with a higher risk of corrosion initiation [12,13]. Additionally, the moisture conditions within these voids have been shown to affect the risk of corrosion initiation [14,15].

Numerical studies on the corrosion and cracking processes in RC further indicate that transport of corrosion products through cracks and pore networks influences the extent of structural damage [7,16,17]. Although direct experimental data on this transport process are limited, the presence of corrosion stains on the surface of reinforced concrete specimens (see for example [16,18,19]), suggests that understanding the transport of corrosion products is important for addressing progressive deterioration.

In addition to quantifying properties of corrosion and its associated processes that serve as input for corrosion models, validation of these models is essential to ensure their accuracy. Validation can be achieved by, for example, comparing experimental results and modelling predictions on the time-to-corrosion-cracking [5], crack patterns [7], crack width versus steel loss [8] and bond performance [6]. To validate these numerical models, it is crucial to obtain high quality experimental data which describe the *evolution* of corrosion within the specimen, capturing also damage and fracture in the three-dimensional (3D) space.

In recent years, X-ray and Neutron Computed Tomography (XCT and NCT) have been increasingly employed for studying cementitious materials [20,21]. These non-destructive methods provide 3D, and even 4D (3D + time), image data of the sample for subsequent qualitative and quantitative analyses. Complementary information of the sample is obtained, by integrating XCT and NCT data in multimodal analyses, exploiting the distinct interactions of X-rays and neutrons with matter [22,23].

In the domain of concrete, the integrated use of XCT and NCT has enabled the identification of relevant material phases such as cement paste, sand and aggregates, steel and corrosion products, as well as determination of corroded sections in the steel [24–27]. Furthermore, XCT and NCT can be used as a base for computational analyses for various purposes.

For instance, previous studies on characterisation on the type of corrosion products within the samples quantified the volumetric expansion coefficient to 3.90 [28] and 3.91 [25] under accelerated corrosion conditions. The close agreement between these two independent studies highlights the consistency of the findings. For natural corrosion, slightly higher values of 4.13 and 4.24 were reported [25]. Further research is needed to verify these findings for different conditions, and to improve their statistical significance.

While XCT and NCT provide data on the evolving internal structure of the sample, there is no information about materials transported from the specimen. A logical next step would be to characterise the composition of the water surrounding the samples to identify corrosion products. Inductively Coupled Plasma Mass Spectrometry (ICP-MS) offers a precise measure of the elemental composition of a substance [29]. Therefore, ICP-MS is used in the current study to quantify the amount of corrosion products transported out of the specimen by analysing the concentration of iron isotopes in the surrounding water during the accelerated corrosion process. Furthermore, by combining ICP-MS with electrical resistance measurements, the relationship between transport of corrosion products and the development of concrete cracking can be studied.

Table 1
Material composition and strength of the different mortars.

	Mortar B	Mortar C
Specimen IDs	NX10B, TC10B1-3	NX10C, TC10C1-3
Mortar composition		
Cement [kg m^{-3}]	480	
Water [kg m^{-3}]	240	
Sand [kg m^{-3}]	1500	
NaBr [% by mass of cement]	3	–
NaCl [% by mass of cement]	–	3
Material strength		
Compressive strength [MPa]	33.9 ± 0.25	35.6 ± 1.2
Tensile strength [MPa]	3.0 ± 0.2	3.3 ± 0.2
Fracture energy [N m^{-1}]	60.9 ± 4.2	69.2 ± 8.2

The aim of the present research is therefore to characterise steel corrosion and to quantify damage in small-scale laboratory-made specimens under accelerated corrosion conditions. This is achieved by monitoring the accelerated corrosion experiments with a combination of electrical resistance measurements, image-based approaches (NCT and XCT) and analytical techniques (ICP-MS). The work aims to achieve and correlate the following analyses:

- To quantify the free volumetric expansion coefficient of the corrosion products;
- To analyse the corrosion morphology and its relation to mortar cracking and macroscopic interfacial voids;
- To study the effect of macroscopic interfacial void size on the risk of pitting corrosion in these regions;
- To estimate the volumetric strain in the corrosion layer;
- To measure corrosion-induced damage within the mortar cover;
- To investigate the effect of transport of corrosion products through mortar cracks during the accelerated corrosion process.

2. Specimens and methods

The experimental campaign involved two series of specimens, NX10 and TC10. The NX10 specimens were studied through combined Neutron and X-ray Computed Tomography (NCT and XCT), acquired before and after accelerated corrosion. Details about the NX10 series are further elaborated in Section 2.1. The TC10 specimens were designed to study the interaction between mortar cracking and transport of corrosion products from these cracks during the accelerated corrosion process. For the chemical analysis of transported corrosion products, Inductively Coupled Plasma Mass Spectrometry (ICP-MS) was used. Further information on the TC10 series is provided in Section 2.6.

All cylindrical specimens measured 26 mm in diameter and 30 mm in length. Each specimen contained a centrally positioned, plain steel rod with a diameter of 6 mm. The steel rods were manufactured from an 8 mm ribbed reinforcement bar, whose ribs were removed using a lathe. The cement used was of type CEMII/A-LL 42.5R [30], and the sand was made from crushed stone, and was ranging from 0 to 6 mm in size. A superplasticiser was added to ensure a proper workability of the fresh mortar mixes. All mortar specimens, including those for the NX10 and TC10 series as well as the strength tests, were compacted using a vibrating table to ensure uniform density and reduce entrapped air. The composition and strength parameters of the two mortars used in the experiment are specified in Table 1.

To prevent the formation of a thin oxide layer around the steel bars, which initially protects against corrosion [2], sodium bromide was added to mortar B (and corresponding specimens NX10B, TC10B1-3). Specimens NX10C and TC10C1-3 (mortar C) were instead cast with sodium chloride. The use of different types of salts was motivated by their different neutron attenuation coefficients. Chlorides, with large neutron attenuation [23], tend to increase the noise level in the NCT

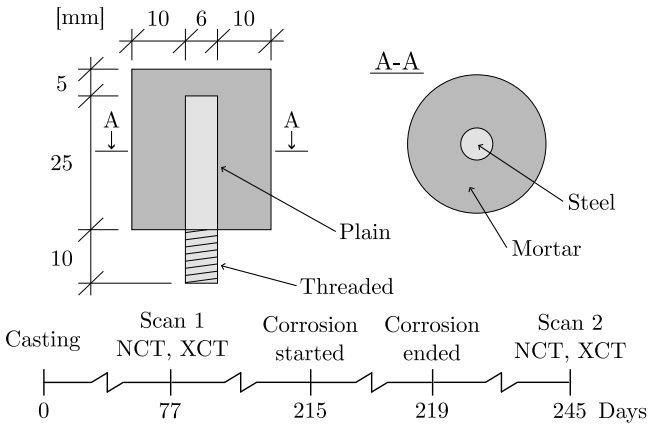

Fig. 1. Drawing of the sample geometry and timeline of the experimental campaign for specimens in series NX10.

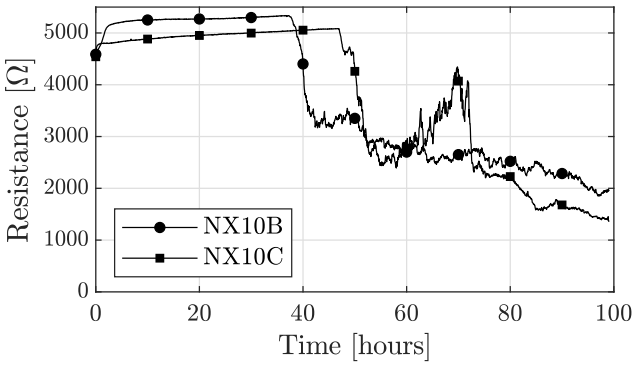

Fig. 2. Electrical resistance measurements of the specimens during the accelerated corrosion process.

scans. Consequently, some of the specimens were cast with sodium bromides, which exhibit lower neutron attenuation, to investigate the impact of different salt additives in mortar mixes on the quality of the NCT data.

The strength properties of the material were measured 28 d after casting. The compressive strength was measured following the guidelines in [31] using three cylindrical specimens, each with a diameter of 100 mm and a length of 200 mm. The fracture energy was measured through a wedge splitting test [32], conducted on three cubic specimens with a side length of 150 mm, using displacement-controlled loading at a rate of 0.2 mm s^{-1}. The tensile strength was estimated based on the wedge splitting tests. Specifically, for each specimen in the series, the tensile strength was estimated through an inverse cross-sectional analysis of the uncracked specimen. In this analysis, the tensile stress directly beneath the notch tip was estimated using the splitting force from the wedge splitting test.

2.1. Neutron and X-ray computed tomography

Two cylindrical reinforced mortar samples, NX10B and NX10C, were manufactured and Neutron and X-ray Computed Tomography (NCT and XCT) were acquired at the NeXT Instrument at the Institut Laue-Langevin [33] at two different stages - prior to and after accelerated corrosion, see Fig. 1.

After casting, the specimens were immersed in water for curing and storing until the first scans with NCT and XCT, carried out 77 d after casting. Although this period is not negligible for the possible formation of natural corrosion, no corrosion products were observed in the imaging data from the first scan. Therefore, any spontaneous corrosion that may have formed during this time was below the resolution of the imaging data. Prior to the second scan, carried out 245 d after casting, the specimens were subjected to accelerated corrosion.

The neutron instrument was configured with a nominal voxel size of 16.8 µm and a field of view of 32 mm × 32 mm. This was achieved by coupling a 160 mm Heliflex lens with a 50 mm Canon f./1.2 lens in an infinity-corrected optics setup. Images were acquired with a Hamamatsu Orca 4V3. A 20 µm Gadolinium scintillator and a 10 mm pinhole, positioned 10 m from the sample, were used to produce a neutron penumbra similar to the voxel size, resulting in a true resolution close to 20 µm. A total of 1216 projections were acquired with a parallel beam over a 360° rotation of the sample, with each projection being the median of 3 individual radiographs, each 5 s long. A filtered-back projection algorithm was used for tomographic reconstruction.

The X-ray source operated at a current of 130 µA and a voltage of 140 kV. The nominal voxel size was of 18.7 µm with a field of view of 32 mm × 40 mm. 1216 cone-beam projection were acquired over a 360° rotation of the sample, each the result of the average of seven individual radiographs. A copper filter was placed in front of the X-ray source, to reduce beam hardening artifacts, caused by lower-energy X-rays. Furthermore, the image intensities were normalised in the XCT data, to correct for the beam hardening in the reconstructed dataset, using the method outlined in [34].

2.2. Accelerated corrosion

Corrosion of the steel bars was induced using impressed current. Specimens cast with sodium bromide, NX10B and TC10B1-3, were placed in separate plastic containers filled with a water solution containing 3% sodium bromide, while specimens cast with sodium chloride, NX10C and TC10C1-3, were immersed in a water solution containing 3% sodium chloride. The positive terminal was connected to the reinforcing steel (the anode) and the negative terminal was connected to a copper mesh (the cathode) surrounding the specimen to close the electrical circuit. In order to mimic the process of natural corrosion, the current density was set to 50 µA cm^{-2}, which is considered acceptable [35]. The current was kept constant for a period slightly less than 100 h using a custom-made constant current source that adjusted the electrical potential when the resistivity in the sample changed. The electrical resistance in the circuit was monitored by logging of the electrical potential, and the measurements are shown in Fig. 2.

2.3. Volumetric expansion coefficient of corrosion products

The volumetric expansion coefficient of corrosion products in the mortar samples was evaluated from the XCT. For this estimation, macroscopic interfacial voids partially filled with corrosion products were identified. The volume loss of steel was estimated by calculating the difference between the initial volume obtained from the tomography scan before corrosion and the remaining volume measured from the scan after corrosion. A similar approach was employed to estimate the volume of corrosion products in voids, where changes in greyscale values within the voids were analysed.

These changes correspond to changes in the density of the material accumulated within the void, as X-ray attenuation generally increases with the density of the material. These variations in greyscale levels, illustrated in Fig. 3, were ascribed to the accumulation of corrosion products. The estimation was performed in all dimensions of the 3D dataset, considering all cross-sectional images in the 2D space containing this void. By computing the volume loss of steel, $\Delta V_{s,pore}$, and the volume of uncompressed corrosion products, $V_{c,pore}$, the volumetric expansion coefficient, η, was calculated as

$$\eta = \frac{V_{c,pore}}{\Delta V_{s,pore}} \tag{1}$$

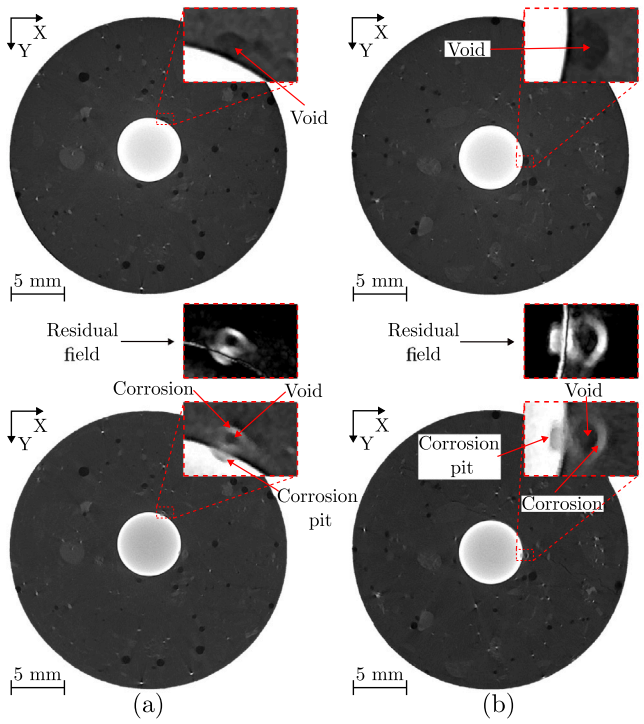

Fig. 3. Horizontal slices of X-ray Tomographies revealing partially filled voids at the SCI, used for estimation of the volumetric expansion coefficient. Top and bottom rows: before and after corrosion, respectively. (a) NX10B and (b) NX10C.

2.4. Volumetric strain in the corrosion layer

The XCT and NCT datasets were spatially aligned by computing a linear transformation matrix for each dataset. This alignment process was validated by calculating the isotropic strain tensors derived from these transformation matrices. The resulting isotropic strains were found to be small, less than one percent for all datasets, indicating successful alignments.

Following the alignment process, phase segmentation of each sample was performed. This segmentation facilitated the estimation of the volumetric strain in the corrosion layer, based on the relationship between the volume of compressed corrosion products and their free volume expansion, as introduced in [26]. This volumetric strain was calculated using the expression

$$\varepsilon_v = \frac{V_{cc}}{\eta \Delta V_s - V_{ca}} - 1 \tag{2}$$

where V_{cc} represents the volume of compressed corrosion in the sample, η is the volumetric expansion coefficient of corrosion products (detailed in Section 2.3), ΔV_s denotes the volume loss of steel and V_{ca} is the volume of uncompressed corrosion products accumulated in voids. It is worth noting that in the derivation of this expression, it is assumed that no corrosion products are transported out of the specimen. This assumption and its implications are further discussed in Section 3.2.

To estimate the variation of the volumetric strain in the corrosion layer, the sample was divided into radial and axial segments. Specifically, the sample was partitioned into sections of fixed angular spans around the circumference ($\Delta\theta = \frac{\pi}{16}$) and over a specific length ($dL =$ 0.25 mm) along the steel bar.

2.5. Digital volume correlation

A Local Digital Volume Correlation (DVC) [36] was performed on the tomographies, in order to measure deformations within each sample. For these DVC analyses, the neutron data was considered, due to the higher contrast between the constituting phases (pores, cement paste and sand), compared to the XCT. In a Local DVC, the reference (uncorroded) configuration of the sample is divided into regular subsets. Each subset was then cross-correlated with the corresponding subset in the deformed (corroded) configuration of the sample. This cross-correlation aims to find a displacement function for each subset that describes the transformation from the reference to the deformed configuration. This function is solved iteratively by minimising the sum of the squared image residuals in the subset. This cross-correlation was performed independently for each subset, without imposing continuity between them.

Each subset, representing as a region in the sample in the 3D space of a predefined size, forms a unique pattern of voxels with different greyscale values. The size of this subset is an important parameter, as a smaller subset contains fewer voxels, increasing the uncertainty of the measured displacement, but a too-large subset will fail to capture local deformations.

To ensure convergence, the subset size was optimised, and a size of 81 × 81 × 71 voxels was chosen in the following. At this size, the convergence ratio was 88% and 83% for specimen NX10B and NX10C, respectively. A correction was made for subsets where the cross-correlation was unsuccessful. For these subsets, the displacement was interpolated from nearby subsets using an inverse-distance weighting algorithm to compute the strain field. Prior to this strain calculation, a median filter with a 2 × 2 × 2 stencil was applied to the displacement field.

2.6. Inductively coupled plasma mass spectrometry

While the image data of samples NX10B and NX10C provided information on the propagation of corrosion and deformations inside the specimens, the transport of corrosion products out of the specimens remained unknown. Therefore, to investigate the effect of the transport of corrosion products, Inductively Coupled Plasma Mass Spectrometry (ICP-MS) was performed to measure the concentration of iron isotopes in the water solution surrounding the specimens during the accelerated corrosion process.

This technique is an elemental analysis method that measures the concentration of elements in the sample [37]. Shortly described, the ICP-MS technique involves the following steps: Firstly, the water in the sample is turned into a fine aerosol mist. Secondly, the aerosol mist is introduced in a high-temperature plasma, which ionises the elements in the sample. Thirdly, the ions are directed into a mass spectrometer, where they are separated based on their mass-to-charge ratio. Lastly, the separated ions are detected and counted, providing insight on their relative quantities.

In this study, ICP-MS was used to measure the concentration of the isotope Iron-57, based on practical considerations. The isotopic composition of non-radioactive naturally occurring elements, such as Iron-57, was expected to remain consistent between standard tests and the present samples. This ensured that any observed variations in Iron-57 abundance primarily reflected changes in the concentration of iron isotopes rather than the isotopic compositions. Moreover, Iron-57 was selected due to its reduced susceptibility to spectral interference compared to other iron isotopes, which simplified the analysis process and enhanced the measurement accuracy.

For specimens NX10B and NX10C, a single water sample was taken at the end of the accelerated corrosion period. For specimens in test series TC10B and TC10C, the concentration of Iron-57 was monitored by taking water samples at multiple intervals during the corrosion process. The water sampling strategy was as follows. Before applying any current to the specimens, one water sample was taken from each specimen to measure the initial concentration of Iron-57 in the water. Thereafter, electrical current was applied, and water samples were taken every working day. A single volume pipette was used to sample 1 mL from the saline water solution for each water sample collected.

Deionised water was added to the containers to ensure that the volume of water surrounding the specimens, hence the concentration of salt, remained stable throughout the accelerated corrosion period. The water, in which each specimen was immersed, was carefully mixed to evenly disperse any sedimented corrosion products, to ensure a representative measure of the concentration of Iron-57. Subsequently, after water samples were taken, the samples were diluted by adding 24 mL of deionised water, resulting in a dilution factor of 1:25. The dilution was necessary to prevent salt from suppressing signals in the ICP-MS analysis [38]. Lastly, 1% of nitric acid was added to the collected water samples to make sure that all particles of corrosion products were dissolved. The water samples were sealed and stored at a constant temperature of 8 °C until the ICP-MS was performed.

3. Results and discussion

In the following section, the results from the study are presented. Starting with the sample preparations, the use of sodium bromide in the fresh mortar mix for NX10B had no clear effect on the noise level in the NCT scan compared to NX10C, which was cast with sodium chloride. Although the attenuation of neutrons by bromide is less than that by chloride, noise was observed in the NCT due to the high moisture content within the specimen, masking any potential relative effects of bromide or chloride on the quality of the NCT scan. This highlights a trade-off in the current application: while drying the specimens prior to scanning could have reduced the attenuation of neutrons by hydrogen, improving image quality, it carries the risk of inducing shrinkage cracking. In this case, the decision was to scan the samples without prior drying, which resulted in higher moisture content that decreased the signal-to-noise ratio of the NCT scan.

The electrical resistance measurements of specimens in the NX10 series (Fig. 2), clearly show a drop in electrical resistance, indicating cracking of the mortar. For NX10B, the resistance increased slightly during the initial hours of impressed current and remained stable thereafter, until a sudden drop after 37 h. Subsequently, the resistance gradually decreased.

The resistance of NX10C increased slightly for a period of 47 h before dropping. Unlike NX10B, the resistance of NX10C partially recovered before a second drop occurred. This might be attributed to a gradually developing crack pattern that fully propagated through the cover at the time of the second drop in resistance.

After the accelerated corrosion process, the samples were visually inspected but no surface cracks could be identified in any of the specimens. Furthermore, no signs of corrosion products were observed on the surfaces of the specimens or in the water surrounding the specimens during the accelerated corrosion process.

The results align with other observations from the experiment. Although no cracks could be seen on the surfaces of the specimens, the acquired neutron and X-ray scans revealed cracking in both scanned specimens, as had been indicated by the electrical resistance measurements. The locations of these cracks are consistent with increased damage in the mortar as deduced by DVC analyses (Section 3.5). In addition, ICP-MS analyses (Section 3.2) confirmed that the transport of corrosion products from the specimens at the time of the second tomography scans had a negligible influence.

3.1. Steel corrosion, cracking and macroscopic interfacial voids

The reduction in radius of the steel bar was evaluated using the phase-segmented image data and is shown in Fig. 4a & b, expressed as a function of the angular and axial positions in the bar for specimens NX10B and NX10C, respectively. In these figures, the loss in steel radius is represented by greyscale colourmaps. Additionally, the position of macroscopic interfacial voids is marked by a coloured overlay. The contour lines in the figure represent the extent of these voids in contact with the steel, while their colours are proportional to their total volume. Finally, the plus signs in the figure mark the location of cracks in the mortar in the vicinity of the steel.

The figure highlights how the corrosion morphologies are non-uniform, and are concentrated near cracks and in regions containing macroscopic interfacial voids. For NX10B, the average loss in steel radius for the corroded regions is 39 μm, while the highest loss in steel radius is 0.4 mm, located in a corrosion pit at a distance of 16.2 mm from the left bar end and at an angle slightly smaller than $\frac{3\pi}{4}$ rad. The size of the void at this pit is 0.75 mm^3.

For NX10C (Fig. 4b), corrosion is localised between two longitudinal cracks in the mortar. Similar to NX10B, pitting corrosion is observed in regions with macroscopic interfacial voids. The average loss in steel radius for the corroded regions of NX10C is 52 μm, somewhat higher than for NX10B. The highest reduction in steel radius (0.32 mm) is found in a pit, 22 mm from the left bar end at an angle of approximately π rad. As with NX10B, this pit is also located in a region with a macroscopic interfacial void, although the size of this void is significantly smaller (0.25 mm^3).

It should be noted that, while highly informative, this information is acquired only at two separate points in time and is not sufficient for studying the continuous progression of corrosion before the initiation of the cracking of the mortar. Uncertainty remains whether corrosion initiated within macroscopic interfacial voids, leading to cracking as pits expanded beyond these voids, if corrosion at the SCI alone generated the expansive pressure causing mortar cracking, or if both factors interacted.

An interesting observation in the figure is that not all macroscopic interfacial voids contain corrosion, possibly due to varying moisture content within these voids. Angst et al. [14] suggested that the moisture condition influences where pitting corrosion occurs. Fully or partially saturated voids tend to increase the risk of corrosion initiation within the void, while air-filled voids or those not in direct contact with the steel may lead to corrosion outside the void.

Previous studies have demonstrated that in situ NCT can effectively be employed to detect distinct phases of water accumulation in fractured porous media [39] and analyse moisture distribution in concrete exposed to high temperatures [24]. In the present study, however, no significant differences in greyscale values (i.e., neutron attenuation) between voids prior to corrosion were observed. While this lack of significant variation could suggest similar moisture levels across voids before the onset of corrosion, high noise levels in the datasets may have masked any discernible differences. Consequently, further investigation into this aspect was not feasible. Future research should aim to monitor and quantify moisture content within macroscopic interfacial voids to better understand its impact on corrosion initiation, ensuring improved data quality to mitigate the effects of noise.

Changes in attenuation were assessed by analysing the residual image field from the before and after corrosion scans, as detailed in Section 2.3. Macroscopic interfacial voids were ordered by size as illustrated in the histogram in Fig. 5. In this diagram, the total number of macroscopic interfacial voids is shown in blue, representing voids that did not contain any corrosion products at the time of the initial tomography scans. The red bars indicate the voids that were completely or partially filled with corrosion products after the second tomography scans.

For NX10B, in Fig. 5a, 29 macroscopic interfacial voids where present at the SCI, out of which 22 (76%) had a volume smaller than 0.1 mm^3. After the corrosion propagation period, corrosion products had accumulated in 12 of these voids (55%). Only 24% of the voids at the SCI had a volume larger than 0.1 mm^3, however, almost all of these larger voids contained corrosion products in the subsequent tomography scan.

Although the largest macroscopic interfacial void for NX10C (Fig. 5b) is smaller than that for NX10B, the ratio of voids smaller than 0.1 mm^3 is 78%, which is very close to the ratio for NX10B. Despite this similarity, only 24% of these smaller macroscopic interfacial voids

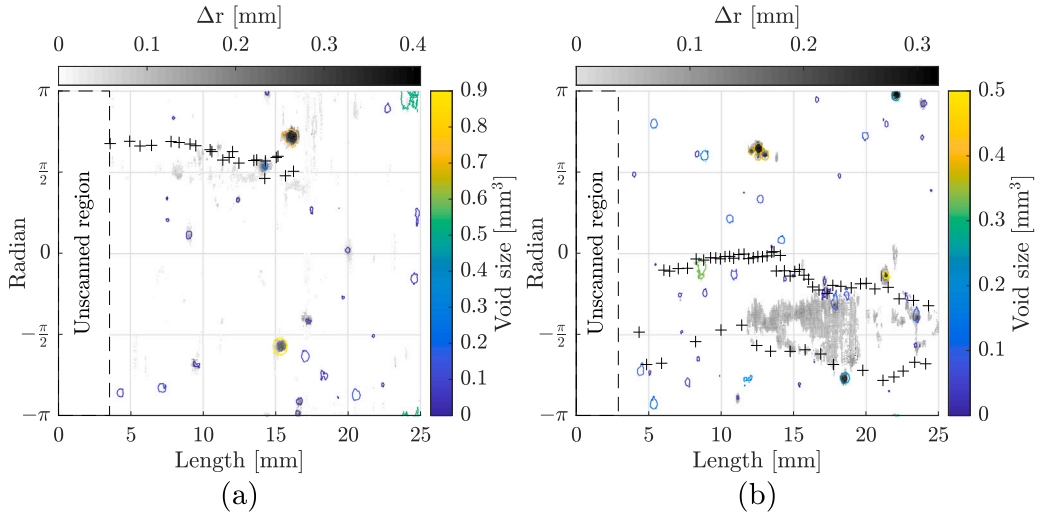

Fig. 4. Loss in steel radius, in greyscale, macroscopic interfacial voids, in colour, and location of mortar cracking at the SCI marked with plus-signs. The plotted size of the voids corresponds to the contact area with the steel while the colour represents their total size. (a) NX10B and (b) NX10C. (For interpretation of the references to colour in this figure legend, the reader is referred to the web version of this article.)

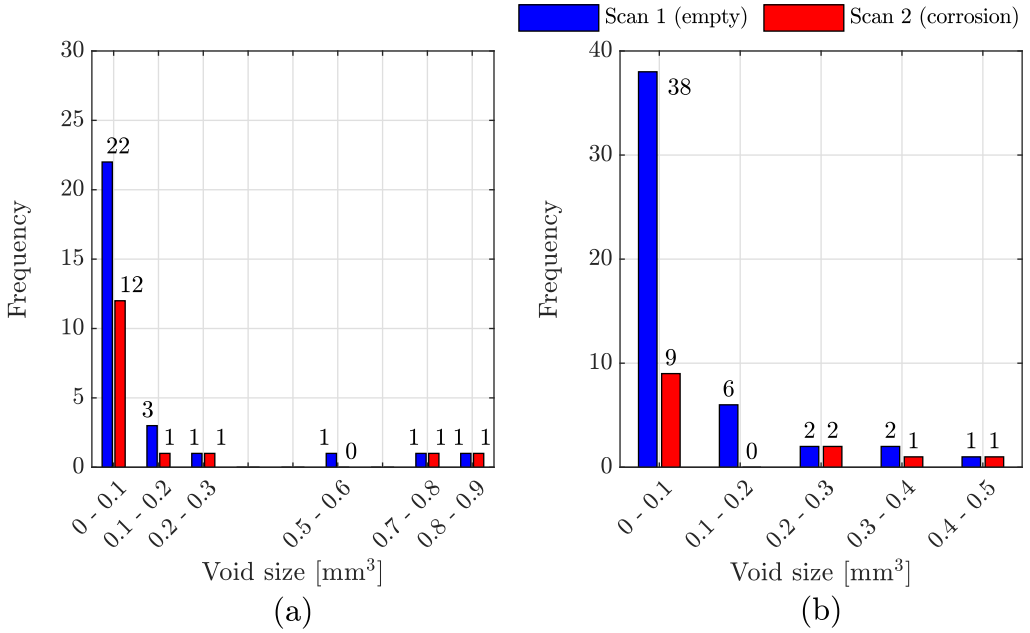

Fig. 5. Distribution of macroscopic interfacial void sizes at the SCI for (a) NX10B and (b) NX10C, showing empty voids (in blue) and voids containing corrosion products after the corrosion period (in red). (For interpretation of the references to colour in this figure legend, the reader is referred to the web version of this article.)

were prone to accommodate corrosion products, a significantly lower percentage than for NX10B. The trend of corrosion accumulation in voids larger than 0.1 mm^3 was similar to that in NX10B, except for voids sized 0.1 to 0.2 mm^3, where none contained any corrosion products after the second scan. These results are consistent with prior research, where it was found that the risk of corrosion initiation in voids at the SCI increases as the void size increases [12,13].

3.2. Transport of corrosion products through cracks during accelerated corrosion

Figs. 6 and 7 show the electrical resistance measurements (solid line, left-hand axes) and the concentration of Iron-57 in the water surrounding the specimens (dashed line, right-hand axes), as a function of time during the corrosion process, for specimens TC10B1-3 and TC10C1-3, respectively. In these figures, the concentration of Iron-57 has been estimated using linear interpolation between the measurement points (circular markers), while the electrical resistance was monitored at a frequency of 20 measurements per hour. The figures also include a single measurement of the Iron-57 concentration, taken before the second tomography scans, for comparison. Top-view images along time are added for some of the specimens to visually support the interpretation of the transport of corrosion products.[1]

During the first four days of the experiment, the concentration of Iron-57 remained low for all specimens except for TC10B2, where the

[1] In the top-view images of specimen TC10C2 (Fig. 7), a red electrical cable can be seen in the upper right corner. This cable might be mistaken for corrosion products; however, it is part of the experimental setup and does not represent actual corrosion.

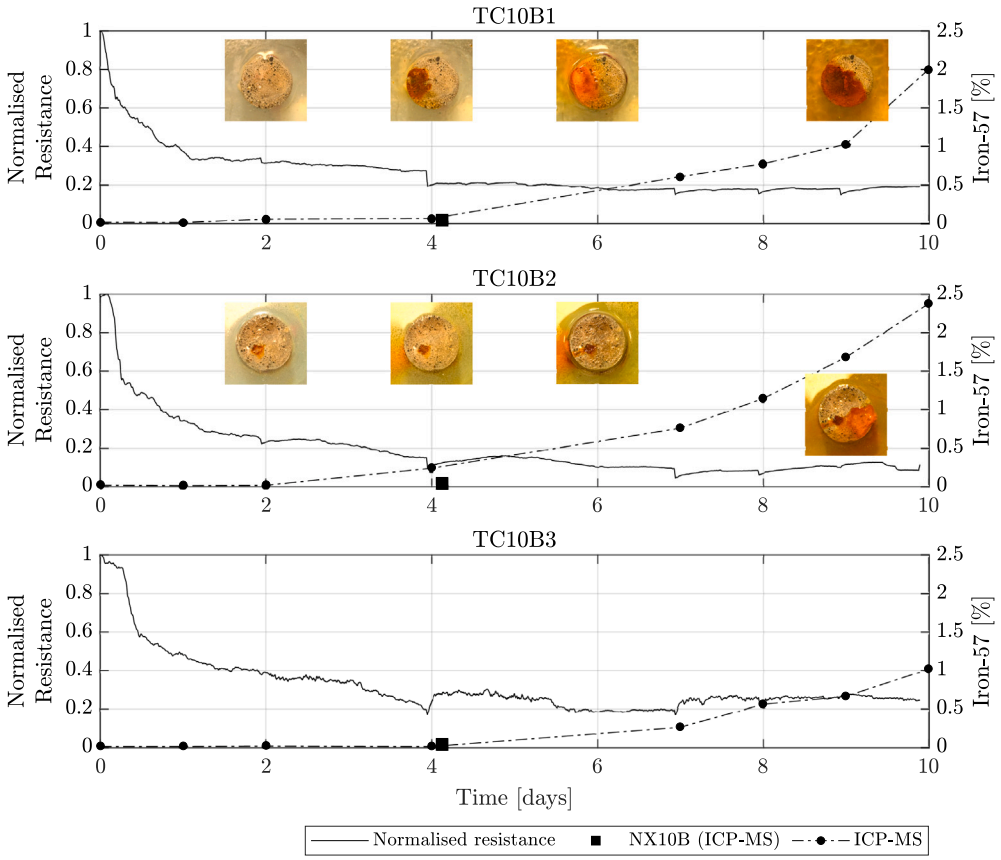

Fig. 6. Electrical resistance and Iron-57 concentration in the water surrounding specimens TC10B1-3 as a function of time. A single Iron-57 measurement (square) from the surrounding water of specimen NX10B at the time of the second tomography scans is also shown. The figure also reports top-view images of TC10B1-2 at 2, 4, 6 and 9 days of accelerated corrosion. (For interpretation of the references to colour in this figure legend, the reader is referred to the web version of this article.)

concentration started to increase already after two days of impressed current. The top-view image of TC10B2 confirms the transport of corrosion products out of the specimen at this time, as corrosion products were visible on the top surface of the specimen.

For all other specimens, the concentration of Iron-57 in the water started to increase after four days of impressed current. This observation is also supported by the top-view images, which show corrosion products in the water and on the surface of the specimens from day four and onwards. By the final day, the concentration of Iron-57 was higher for specimens in the TC10B series compared to TC10C.

It should be noted, however, that the length of the corrosion period varied slightly for the different tests. For specimens TC10B, the accelerated corrosion period lasted for ten days, while the period for TC10C lasted for nine days. The average concentration of Iron-57 isotopes, after nine days, was 1.12% for TC10B, while the average concentration for TC10C was significantly lower at 0.56%.

The electrical resistance measurements for the TC10B specimens (Fig. 6) dropped rapidly during the initial day of impressed current. Additionally, noticeable drops in resistance signals were observed after four and seven days for each specimen, indicating the presence of interference. This suggest that the TC10B specimens may have been connected to the same current source, affecting their individual resistance readings.

Interestingly, a delay in the increase of the concentration of Iron-57 is observed when compared to the initiation of the crack in the mortar. This delay was likely due to a combination of factors: the initial crack width may have been insufficient for corrosion products to be transported out of the specimen, and there may have been a time delay associated with the transport of these corrosion products through the crack. A previous study employing non-linear ultrasonic technique has also suggested a possible delay in the transport of corrosion products relative to mortar cracking [40].

At the time of the second tomography scans, the concentration of Iron-57 in the water was low for specimens NX10B and NX10C. This low concentration supports the assumption that the transport of corrosion products through cracks was negligible during the period prior to the scan and corroborates the assumption made when computing the volumetric strain in the corrosion layer.

3.3. Volumetric expansion coefficient of corrosion products

The volumetric expansion coefficient of the corrosion products was quantified from the XCT data using Eq. (1). For this quantification, the partially filled voids shown in Fig. 3 were analysed. The selection of partially filled macroscopic interfacial voids was crucial, as the methodology for quantifying this coefficient (Section 2.3) relies on the volume balance between the (bulk) volume of accumulated corrosion products in the void and on the volume loss of the neighbouring steel. If the voids are completely filled with corrosion products, the estimation of the bulk volume is affected by the possible compaction of corrosion products within the void. This was not the case for the voids considered here.

The volumetric expansion coefficient of corrosion products was determined to be $\eta = 3.90$ for NX10B, and $\eta = 3.84$ for NX10C. These values suggest that the corrosion products could be either Iron(II) hydroxide, $Fe(OH)_2$ ($\eta \approx 3.75$), or Iron(III) hydroxide, $Fe(OH)_3$ ($\eta \approx 4.1$) [2], or a mix of both. The values are higher than the reference value of around two, which is often assumed in the modelling of the corrosion

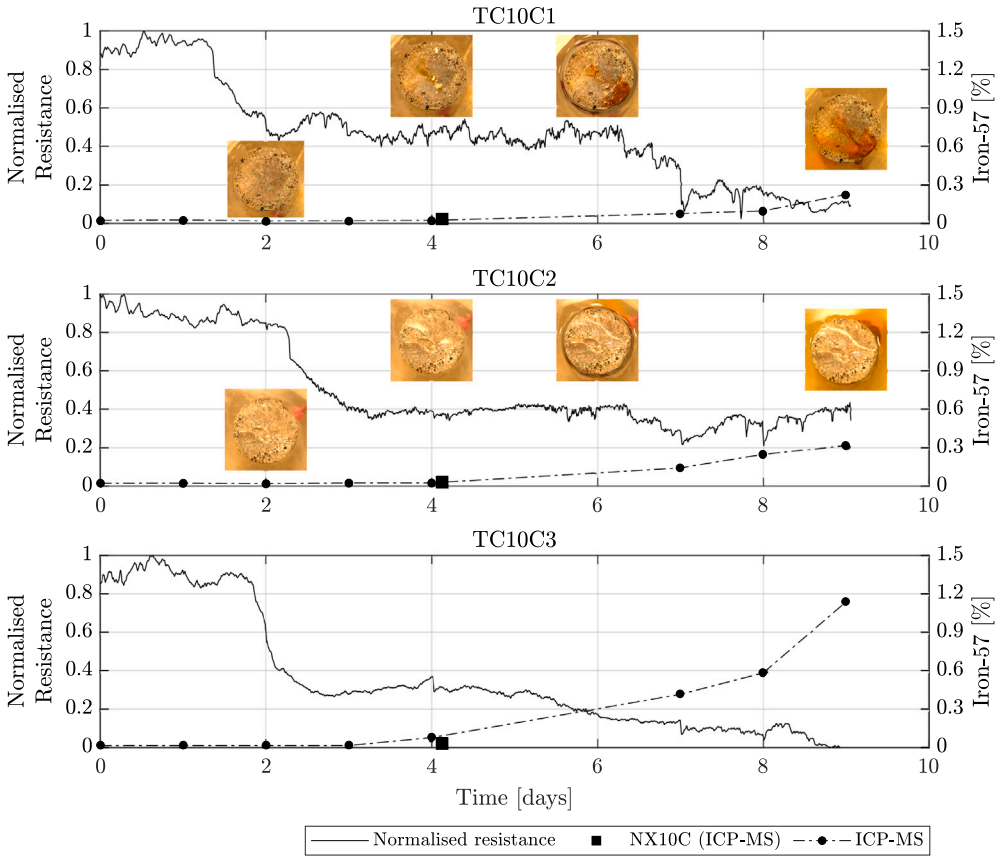

Fig. 7. Electrical resistance and Iron-57 concentration in the water surrounding specimens TC10C1-3 as a function of time. A single Iron-57 measurement (square) from the surrounding water of specimen NX10C at the time of the second tomography scans is also shown. The figure also reports top-view images of TC10C1-2 at 2, 4, 6 and 9 days of accelerated corrosion. (For interpretation of the references to colour in this figure legend, the reader is referred to the web version of this article.)

and cracking process. However, the coefficients found in the present paper closely align with previous research quantifying this factor from image-based data and accelerated corrosion conditions, see [25,28].

It is important to stress that the estimation of the volumetric expansion coefficient of corrosion products within a macroscopic interfacial void might not be representative of the entire sample. It has previously been reported that various types of corrosion products have been formed within a single specimen [10], potentially attributed to varying environmental conditions within the sample.

3.4. Volumetric strain in the corrosion layer

Fig. 8 illustrates the volumetric strain in the corrosion layer, estimated using Eq. (2) and the volumetric expansion coefficient of corrosion products determined in Section 3.3 for each sample. The black contour lines mark the contact area of macroscopic interfacial voids with the steel, following a similar procedure to that in Fig. 4.

The volumetric strain in the corrosion layer is relatively large for both specimens, with values ranging from approximately −0.6 to −0.8 for most regions. It is important to emphasise that these observed strain magnitudes are strongly influenced by the type of corrosion products formed within the sample. This aspect is considered in Eq. (2) by the volumetric expansion coefficient of corrosion products, which was found to be relatively high in this study. For a lower volumetric expansion coefficient, the measured strains would have been significantly reduced, as demonstrated in [26].

In vicinity of some macroscopic interfacial voids, the values are non-zero, which is unreasonable under the assumption that corrosion products expanded freely in these regions. These non-zero values of the volumetric strain of corrosion products near macroscopic interfacial voids were due to numerical errors when the region containing these voids were divided into multiple elements. Additionally, it should be noted that the partial volume effect, common in imaging, may have introduced some uncertainty in the measurement of the volumetric strains within the sample.

The average volumetric strain for the entire sample was $\bar{\varepsilon}_v = -0.69$ and $\bar{\varepsilon}_v = -0.68$ for NX10B and NX10C, respectively. Although these values are large, they are consistent with previous research findings computing the volumetric strain from the same methodology of phase segmentation and measures of volume balances [26].

3.5. Deformations within the cover of the mortar

Fig. 9 presents renderings of the XCT of the two specimens after the accelerated corrosion process (top) and the corresponding filtered displacement fields (bottom). Surface cracks are visible in both specimens. In this view, the crack in specimen NX10B can be seen to propagate longitudinally, while specimen NX10C exhibits a crack propagating in the transverse direction. The latter observation is noteworthy and unexpected, as corrosion-induced cracks typically propagate in the longitudinal direction of the steel. The presence of cracks in the specimens correlates well with the observed behaviour of the electrical resistance measurement (Fig. 2), where sudden drops, indicating a sudden change in resistivity of the samples, were recorded.

The displacement field of NX10B reveals the presence of the longitudinal crack. The width and orientation of this crack varies along the specimen. Similar local damage was also observed for NX10C.

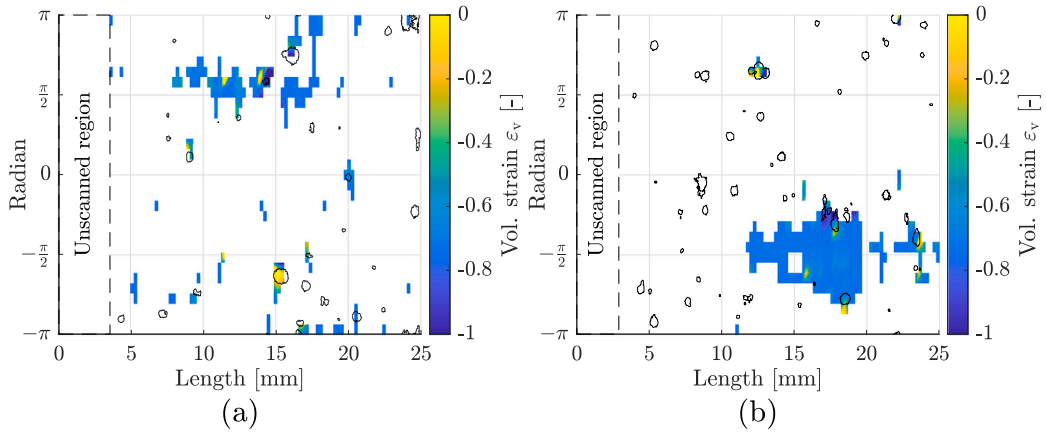

Fig. 8. Volumetric strain in the corrosion layer for (a) NX10B and (b) NX10C (coloured) and the location of macroscopic interfacial voids (black). (For interpretation of the references to colour in this figure legend, the reader is referred to the web version of this article.)

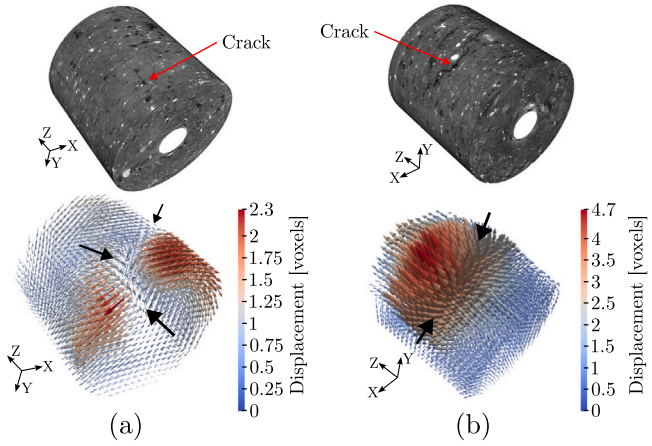

Fig. 9. Rendering of the XCT acquired after corrosion (top) and displacement field (bottom) for (a) NX10B and (b) NX10C. (For interpretation of the references to colour in this figure legend, the reader is referred to the web version of this article.)

In Fig. 10, the orientation of the cracks at the surface of the two specimens are shown for a 3D rendering of each specimen. Arrows mark the location of mortar cracks as visible from the images. Furthermore, two cross-sectional slices of each specimen are shown along with the corresponding distribution of first principal strains (mid and bottom, respectively). For specimen NX10B and cross-section A–A, one radial crack is visible, and strain localisation can be seen in correspondence with this crack, which confirms the reliability of the DVC results. For cross-section B-B, the crack is partly identifiable at the surface and is hard to identify in the cross-section.

For specimen NX10C, a transverse crack is observed in between two longitudinal cracks, which are not as clearly visible. It is reasonable to assume that this transverse crack formed as to accommodate the dominant longitudinal cracking, most likely induced by a local weakness in the mortar. Similar to NX10B, strain localisation was measured in regions where cracks could be identified from the image data. The results from the DVC are consistent with previous studies [26,41], supporting the methodology as such for measuring corrosion-induced deformations.

4. Conclusions

This study demonstrated a high level of consistency between a variety of complementary measurements and visual observations. Electrical resistance measurements indicated mortar cracking, although no cracks were visible to the naked eye. However, this cracking was confirmed through X-ray and Neutron Computed Tomography imaging which was further corroborated by the strain fields computed with Local Digital Image Correlation. A delay in the transport of corrosion products relative to the cracking was observed, which was corroborated by analytical measurements of the concentration of Iron-57 in the surrounding water used during the accelerated corrosion process.

The main findings of this work are:

1. The study evaluated the volumetric expansion coefficient of corrosion products in partially filled macroscopic interfacial voids, providing essential input data for modelling of the corrosion and cracking process. This coefficient was estimated to 3.84 and 3.90 for the two specimens, which aligns well with previous research findings on accelerated corrosion conditions.
2. The research highlighted a possible trend between pitting corrosion and macroscopic interfacial voids, where the risk of corrosion was observed to increase with void size.
3. Corrosion products were visually observed to be transported out of the specimens after cracking of the mortar occurred, albeit with some delay. This can likely be ascribed to the limited crack width. Inductively Coupled Plasma Mass Spectrometry and the electrical resistance measurements confirmed this observation. This validates the assumption made when estimating the volumetric strain in the corrosion layer, where the influence of this transportation was assumed to be negligible.
4. Phase segmentations of the samples were achieved using multimodal X-ray and Neutron Computed Tomography. Through this segmentation, the volumetric strain in the corrosion layer was estimated based on a relationship between the volume of compressed corrosion products and their free volume expansion. The average volumetric strain was found to be relatively high in both samples ($\bar{\varepsilon}_v = -0.69$ and $\bar{\varepsilon}_v = -0.68$).

The data collected in this study provides opportunities for calibrating numerical models of the corrosion and cracking processes. Future experimental research should involve conducting multiple scans of the samples at various stages throughout the corrosion process. This approach will enable a more detailed, time-resolved study of steel corrosion in reinforced concrete.

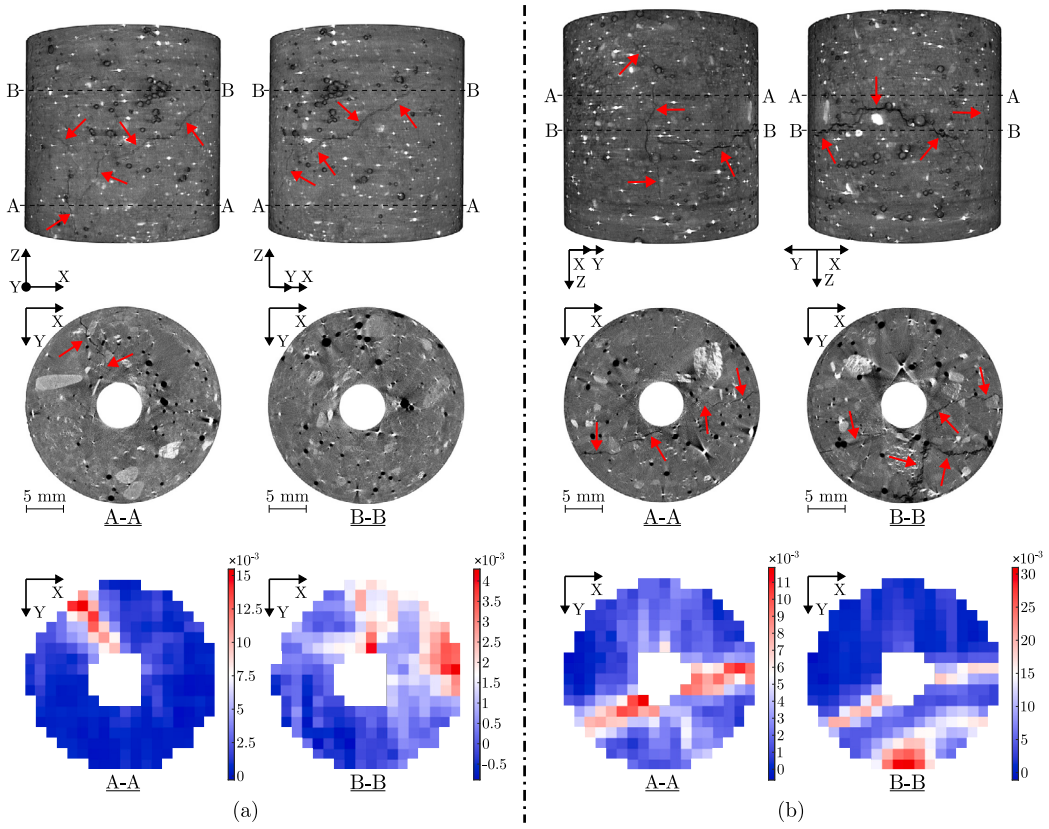

Fig. 10. Illustration of the orientation of mortar cracks at the surface (top), cross-sectional slices at different locations in the samples (mid) and the corresponding distribution of the first principal strain for (a) NX10B and (b) NX10C. Please note the different scales in the colourbars. (For interpretation of the references to colour in this figure legend, the reader is referred to the web version of this article.)

CRediT authorship contribution statement

Andreas Alhede: Writing – review & editing, Writing – original draft, Visualization, Investigation, Formal analysis, Conceptualization. **Jelke Dijkstra:** Writing – review & editing, Supervision, Investigation, Funding acquisition, Conceptualization. **Alessandro Tengattini:** Writing – review & editing, Investigation, Data curation. **Karin Lundgren:** Writing – review & editing, Supervision, Investigation, Funding acquisition, Conceptualization.

Funding

This project was financially supported by the Swedish Research Council Formas (grant no. 2022-01175) and the Swedish Transport Administration, Sweden (grant no. 2021/27819).

Declaration of competing interest

The authors declare that they have no known competing financial interests or personal relationships that could have appeared to influence the work reported in this paper.

Acknowledgements

The authors would like to acknowledge Institut Laue Langevin (ILL) for granting the possibility to carry out the experimental work at the NeXT beamline (experiment 1-07-1). The computations were enabled by resources provided by the National Academic Infrastructure for Supercomputing in Sweden (NAISS), partially funded by the Swedish Research Council through grant agreement no. 2022-06725. The authors would also like to acknowledge Research Specialist Amir Saeid Mohammadi and Professor Sebastien Rauch, both from the Division of Water Environment Technology at Chalmers University of Technology, for their assistance with the ICP-MS analysis. Lastly, Sebastian Almfeldt, Senior Research Engineer at Chalmers University of Technology, is acknowledged for his lab assistance, and Katja Frid, Head of Department of Material Science and Applied Mathematics, Malmö University, for assisting with the mortar mix design.

Data availability

The image data used in this study are made available at: https://dx.doi.org/10.5291/ILL-DATA.1-07-1 after the embargo period (14-11-2028)

References

[1] U. Angst, et al., The steel-concrete interface, Mater. Struct. 50 (2017) 143, http://dx.doi.org/10.1617/s11527-017-1010-1.
[2] K. Tuutti, Corrosion of steel in concrete, Swed. Cem. Concr. Res. Inst. Stock. (1982).
[3] E. Chen, C. Berrocal, I. Löfgren, K. Lundgren, Corrosion pattern and mechanical behaviour of corroded rebars in cracked plain and fibre reinforced concrete, Fibre Reinf. Concr.: Improv. Innov. 30 (2020) 477–488, http://dx.doi.org/10.1007/978-3-030-58482-5_44.
[4] W. Zhang, X. Song, X. Gu, S. Li, Tensile and fatigue behavior of corroded rebars, Constr. Build. Mater. 34 (2012) 409–417, http://dx.doi.org/10.1016/j.conbuildmat.2012.02.071.
[5] Y. Liu, R. Weyers, Modeling the time-to-corrosion cracking in chloride contaminated reinforced concrete structures, ACI Mater. J. 95 (1998) 675–681, http://dx.doi.org/10.14359/410.
[6] K. Lundgren, Bond between ribbed bars and concrete. Part 2: The effect of corrosion, Mag. Concr. Res. 57 (2005) 383–395, http://dx.doi.org/10.1680/macr.2005.57.7.383.
[7] J. Ožbolt, F. Oršanic, G. Balabanić, M. Kušter, Modeling damage in concrete caused by corrosion of reinforcement: coupled 3D FE model, Int. J. Fract. 178 (2012) 233–244, http://dx.doi.org/10.1007/s10704-012-9774-3.

[8] C. Van Steen, T. Van Beirendonck, R. Vrijdaghs, M. Hendriks, E. Verstrynge, A two-phased modelling approach for corrosion-induced concrete cracking and bond deterioration in reinforced concrete, Eng. Struct. 294 (2023) 116624, http://dx.doi.org/10.1016/j.engstruct.2023.116624.
[9] A. Jamali, U. Angst, B. Adey, B. Elsener, Modeling of corrosion-induced concrete cover cracking: A critical analysis, Constr. Build. Mater. 42 (2013) 225–237, http://dx.doi.org/10.1016/j.conbuildmat.2013.01.019.
[10] K. Suda, S. Misra, K. Motohashi, Corrosion products of reinforcing bars embedded in concrete, Corros. Sci. 35 (1993) 1543–1549, http://dx.doi.org/10.1016/0010-938X(93)90382-Q.
[11] A. Dehoux, F. Bouchelaghem, Y. Berthaud, Micromechanical and microstructural investigation of steel corrosion layers of variable age developed under impressed current method, atmospheric or saline conditions, Corros. Sci. 97 (2015) 49–61, http://dx.doi.org/10.1016/j.corsci.2015.04.016.
[12] J.-G. Nam, W. Hartt, K. Kim, Effects of air void at the steel-concrete interface on the corrosion initiation of reinforcing steel in concrete under chloride exposure, J. Korea Concr. Inst. 17 (2005) 829–834.
[13] C. Wen, Y. Tian, Z. Mai, J. Hu, G. Wang, Effect of macropores at the steel-concrete interface on localized corrosion behaviour of steel reinforcement, Cem. Concr. Compos. 129 (2022) 104510, http://dx.doi.org/10.1016/j.cemconcomp.2022.104510.
[14] U. Angst, et al., The effect of the steel-concrete interface on chloride-induced corrosion initiation in concrete: a review by RILEM TC 262-SCI, Mater. Struct. 52 (2019) 88, http://dx.doi.org/10.1617/s11527-019-1387-0.
[15] M. Hren, T. Kosec, A. Legat, An investigation into corrosion around voids at the steel-concrete interface, Cem. Concr. Res. 181 (2024) 107545, http://dx.doi.org/10.1016/j.cemconres.2024.107545.
[16] E. Sola, J. Ožbolt, G. Balabanić, M. Mir, Experimental and numerical study of accelerated corrosion of steel reinforcement in concrete: Transport of corrosion products, Cem. Concr. Res. 120 (2019) 119–131, http://dx.doi.org/10.1016/j.cemconres.2019.03.018.
[17] L. Chang, J. Thorsson, K. Lundgren, 3D modelling of the interaction between bending and corrosion-induced cracks in reinforced concrete beams, Constr. Build. Mater. 411 (2024) 134272, http://dx.doi.org/10.1016/j.conbuildmat.2023.134272.
[18] W. Zhu, R. François, C. Zhang, D. Zhang, Propagation of corrosion-induced cracks of the RC beam exposed to marine environment under sustained load for a period of 26 years, Cem. Concr. Res. 103 (2018) 66–76, http://dx.doi.org/10.1016/j.cemconres.2017.09.014.
[19] C. Berrocal, I. Fernandez, R. Rempling, The interplay between corrosion and cracks in reinforced concrete beams with non-uniform reinforcement corrosion, Mater. Struct. 55 (120) (2022) http://dx.doi.org/10.1617/s11527-022-01956-2.
[20] S. Brisard, M. Serdar, P. Monteiro, Multiscale X-ray tomography of cementitious materials: A review, Cem. Concr. Res. 128 (2020) 105824, http://dx.doi.org/10.1016/j.cemconres.2019.105824.
[21] P. Zhang, F. Wittmann, P. Lura, H. Müller, S. Han, T. Zhao, Application of neutron imaging to investigate fundamental aspects of durability of cement-based materials: A review, Cem. Concr. Res. 108 (2018) 152–166, http://dx.doi.org/10.1016/j.cemconres.2018.03.003.
[22] E. Roubin, E. Andò, S. Roux, The colors of concrete as seen by X-rays and neutrons, Cem. Concr. Compos. 104 (2019) 103336, http://dx.doi.org/10.1016/j.cemconcomp.2019.103336.
[23] A. Tengattini, N. Lenoir, E. Andò, G. Viggiani, Neutron imaging for geomechanics: A review, Geomech. Energy Environ. 27 (2021) 100206, http://dx.doi.org/10.1016/j.gete.2020.100206.
[24] D. Dauti, A. Tengattini, S. Dal Pont, N. Toropovs, M. Briffaut, B. Weber, Analysis of moisture migration in concrete at high temperature through in-situ neutron tomography, Cem. Concr. Res. 111 (2018) 41–55, http://dx.doi.org/10.1016/j.cemconres.2018.06.010.
[25] S. Robuschi, A. Tengattini, J. Dijkstra, I. Fernandez, K. Lundgren, A closer look at corrosion of steel reinforcement bars in concrete using 3D neutron and X-ray computed tomography, Cem. Concr. Res. 144 (2021) 106439, http://dx.doi.org/10.1016/j.cemconres.2021.106439.
[26] A. Alhede, J. Dijkstra, S. Robuschi, A. Tengattini, K. Lundgren, A two-stage study of steel corrosion and internal cracking revealed by multimodal tomography, Constr. Build. Mater. 394 (2023) 132187, http://dx.doi.org/10.1016/j.conbuildmat.2023.132187.
[27] U. Angst, E. Rossi, C. Boschmann Käthler, D. Mannes, P. Trtik, B. Elsener, Z. Zhou, M. Strobl, Chloride-induced corrosion of steel in concrete - insights from bimodal neutron and X-ray microtomography combined with ex-situ microscopy, Mater. Struct. 57 (2024) 56, http://dx.doi.org/10.1617/s11527-024-02337-7.
[28] H. Sun, C. Jiang, K. Cao, D. Yu, W. Liu, X. Zhang, D. Xing, F. Zhao, Monitoring of steel corrosion and cracking in cement paste exposed to combined sulfate-chloride attack with X-ray microtomography, Constr. Build. Mater. 302 (2021) 124345, http://dx.doi.org/10.1016/j.conbuildmat.2021.124345.
[29] A. Ammann, Inductively coupled plasma mass spectrometry (ICP MS): a versatile tool, J. Mass Spectrom. 42 (4) (2007) 419–427, http://dx.doi.org/10.1002/jms.1206.
[30] EN 197-1, Cement - Part 1: Composition, Specifications and Conformity Criteria for Common Cement, Comité Européen de Normalisation (CEN), Europe, 2011.
[31] EN 12390-3, Testing Hardened Concrete - Part 3: Compressive Strength of Test Specimens, Comité Européen de Normalisation (CEN), Europe, 2019.
[32] E. Brühwiler, W. Wittmann, The wedge splitting test, a new method of performing stable fracture mechanics tests, Eng. Fract. Mech. 35 (1990) 117–125, http://dx.doi.org/10.1016/0013-7944(90)90189-N.
[33] A. Tengattini, N. Lenoir, E. Andò, B. Giroud, D. Atkins, J. Beaucour, G. Viggiani, NeXT-Grenoble, the Neutron and X-ray tomograph in Grenoble, Nucl. Instrum. Methods Phys. Res. A 968 (2020) 163939, http://dx.doi.org/10.1016/j.nima.2020.163939.
[34] O. Stamati, E. Roubin, E. Andò, Y. Malecot, Phase segmentation of concrete x-ray tomographic images at meso-scale: Validation with neutron tomography, Cem. Concr. Compos. 88 (2018) 8–16, http://dx.doi.org/10.1016/j.cemconcomp.2017.12.011.
[35] C. Alonso, C. Andrade, J. Rodriguez, J. Diez, Factors controlling cracking of concrete affected by reinforcement corrosion, Mater. Struct. 31 (1998) 435–441, http://dx.doi.org/10.1007/BF02480466.
[36] O. Stamati, et al., Spam: Software for practical analysis of materials, J. Open Source Softw. 5 (2020) 51, http://dx.doi.org/10.21105/joss.02286.
[37] R. Thomas, Practical Guide to ICP-MS: A Tutorial for Beginners, third ed., Taylor & Francis Group, 2013.
[38] E. Hywel Evans, J.J. Giglio, Interferences in inductively coupled plasma mass spectroscopy. A review, J. Anal. At. Spectrom. 8 (1993) 1–18, http://dx.doi.org/10.1039/JA9930800001.
[39] A. Nemati, B. Lukić, A. Tengattini, R. Gupta, M. Briffaut, P. Séchet, Rapid in situ neutron tomography and X-ray imaging of vapor condensation in fractured sandstone, Transp. Porous Media 150 (2023) 327–357, http://dx.doi.org/10.1007/s11242-023-02014-3.
[40] M. Climent, M. Miró, J. Eiras, P. Poveda, G. de Vera, E. Segovia, J. Ramis, Early detection of corrosion-induced concrete micro-cracking by using nonlinear ultrasonic techniques: Possible influence of mass transport processes, Corros. Mater. Degrad. 3 (2022) 235–257, http://dx.doi.org/10.3390/cmd3020014.
[41] Y. Tian, H. Jiang, X. Fan, G. Zhang, N. Jin, Q. Zeng, X. Jin, D. Yan, Y. Peng, J. Wang, Corrosion damages of reinforced concrete characterized by X-ray CT and DVC techniques, Constr. Build. Mater. 409 (2023) 134218, http://dx.doi.org/10.1016/j.conbuildmat.2023.134218.